Enhanced tuberculosis diagnosis: microscopic automatic stitching of sputum samples utilizing the SURF feature detector

Nadhya Gita Anggana [a,b,1], Indrarini Dyah Irawati [a,b,2], Suci Aulia [a,b,3,*], Lestari [a,b,4]

[a] School of Applied Science, Telkom University, Main Campus, Jl. Telekomunikasi no. 1, Bandung 40257, West Java, Indonesia
[b] Center of Excellence for Green Technology, Research Institute for Intelligent Business and Sustainable Economy, Telkom University, Main Campus (Bandung Campus), Jl. Telekomunikasi no. 1, Bandung 40257, West Java, Indonesia
[1] nadhyaanggana@student.telkomuniversity.ac.id; [2] indrarini@telkomuniversity.ac.id; [3] suciaulia@telkomuniversity.ac.id;
[4] lestari@student.telkomuniversity.ac.id
* corresponding author

ARTICLE INFO

Article history
Received December 10, 2025
Revised February 8, 2026
Accepted February 12, 2026
Available online May 31, 2026

Keywords
Tuberculosis
Automatic Stitching
SIFT
SURF
Ziehl-Neelsen

ABSTRACT

In conventional tuberculosis diagnosis, 100-300 fields of view (FOVs) must be observed, which can lead to observer fatigue. For both tasks, an automatic stitching framework was developed that extends conventional feature-based transformations by incorporating affine-geometry-based feature matching and RANSAC-based homography refinement, thereby accounting for the unique low-texture morphology and irregular patterns of Mycobacterium tuberculosis in ZN-stained sputum smears. The system was tested on a set of 10 overlapping image pairs with a fixed overlap of 30%. Among the evaluated image pairs, the proposed optimized method achieved a 100% success rate. Objective zero-pixel metric-based quantitative analysis also validated higher transparency quality compared to other methods. The proposed SURF implementation reached a minimum number of 345.263 zero-pixels, outperforming standard SURF (964.247) and SIFT (1.069.687). This improved robustness to rotation and illumination variations made the optimized SURF-affine framework a preferred choice for automatic TB diagnosis systems.

1. Introduction

Tuberculosis (TB) is an airborne infectious disease caused by Mycobacterium tuberculosis (MTB) [1], [2], [3], which primarily affects the human respiratory system and spreads through fine droplets released when a patient coughs or sneezes [4], [5]. Limited access to health care services in some areas results in an inability to modulate sputum exposure during coughing and appears insufficient to stop community transmission [6]. Early and rapid laboratory diagnosis is therefore the key to controlling its spread. The microscopic examination of the sputum with Fluorescence Microscopy (FM) [7], [8], [9], [10] or Conventional Microscopy (CM) [11], which is cheaper, constitutes the mainstay for TB diagnosis in limited-resource settings. However, observation of 100–300 fields of view is still necessary when using a CM-based analysis to check for AFB [12], [13], [14], resulting in labor-intensive, time-consuming operations or observer fatigue. To overcome these limitations, Whole Slide Imaging (WSI) is a widely adopted solution that allows combining multiple full-resolution microscopic images into a single panoramic view [3], [15], [16]. Facilitating WSI is the automatic stitching procedure [17], which overlays images continuously without introducing any structural alterations [18]. The development of feature-based stitching, such as the Scale Invariant Feature Transform (SIFT) algorithm, has greatly improved this field by enabling the detection of local, scale- and rotation-invariant features [14]. While SIFT can produce consistent panoramic images, it often struggles with the irregular patterns, subtle structures, and uneven illumination inherent in sputum smear images. These inconsistencies can lead to unstable keypoint matching, necessitating more robust alternatives to improve the stability of automatic stitching [19], [20], [21], [22].

Since sputum microscopic images inherently involve irregular patterns, subtle structures, and staining differences [23], [24], the keypoint detection algorithms used in automatic stitching should be robust to these variations. In such a noisy setting, conventional flash-and-no-flash algorithms that rely on intensity- or correlation-based stitching may not produce reliable registration. Hence, it would require a feature-based technique with strong robustness to scale, rotation, and illumination changes to accurately merge overlapping fields. The SIFT-based algorithm has been applied to the stitching of tuberculosis microscopic images, and it has been shown that panoramic imaging with acceptable structural consistency can be obtained using SIFT [25]. However, several limitations are also reported, such as the challenge of achieving stable keypoint matching in the presence of diverse backgrounds and non-uniform illumination, which are typical of microscopic samples and sputum smear images. These difficulties underscore the need for stronger alternatives to improve the stability of automatic stitching. For this reason, we subsequently compare SIFT with a well-known feature-based approach to determine which method performs better in the presence of the irregularities observed in sputum microscopy. This requirement leads us to evaluate an advanced feature extractor, viz., Speeded-Up Robust Features (SURF), for the construction of trusted panoramic sputum images [26], [27]. The SURF algorithm aims to detect local image features efficiently and accurately. The SIFT method was a partial inspiration for this algorithm, as it enabled the use of scale-space representations [28]. The advantages of SURF are that it computes object features from images more quickly than other methods and is robust to rotation, scale changes, illumination changes, and viewpoint changes [22]. The SURF algorithm is based on integral image operations and Hessian determinant-based blob detection [29], [30].

Many studies have been conducted to prove the effectiveness of SURF in automatic stitching, with a significant property in being insensitive to light and angle variations [31], [32]. Classic intensity-based methods often lose alignment control when faced with such inconsistency. Moreover, the traditional SIFT algorithm provides an acceptable degree of repeatability but may struggle to maintain stable keypoint matching in sputum images with variable illumination and cluttered backgrounds. Our contribution is to use implemented tools that utilize SIFT-affine or SURF-affine transformations [32], [33]. Unlike traditional applications of SIFT and SURF, our framework includes a RANSAC-based homography refinement followed by a decision node that checks the spatial distribution of keypoint matches to discard unreliable matches. By using affine geometry as a refinement step, the algorithm achieves more accurate registration that compensates for rotation and scaling jitter present in high-resolution microscopy for detecting tuberculosis parasites. A user-defined Zero-Pixel confirms the efficacy of this protocol to quantify the smoothness of the result. This affine-based model provides an efficient and robust diagnostic tool, with a significant reduction in residual artifacts, resulting in a smooth panoramic view for clinical examination. The system uses SURF for robust feature extraction, tailored to the specific morphological considerations of tuberculosis sputum microscopy, to perform automatic stitching. Next, the feature correspondences are detected using a combination of the Brute Force (BF) Matcher, the Avivadi and Lipman approach [17], Lowe's Ratio Test [34], and K-Nearest Neighbors (KNN), and then affine estimators are used to achieve accurate, robust image matching.

2. Method

2.1. System Design

The system design for this study was developed by reviewing the literature on automatic stitching and image processing methods. An automatic stitching technique was used to integrate microscopic images of TB sputum samples during the preparation and evaluation phases in order to preserve image quality. Fig. 1 shows the steps of automatic stitching.

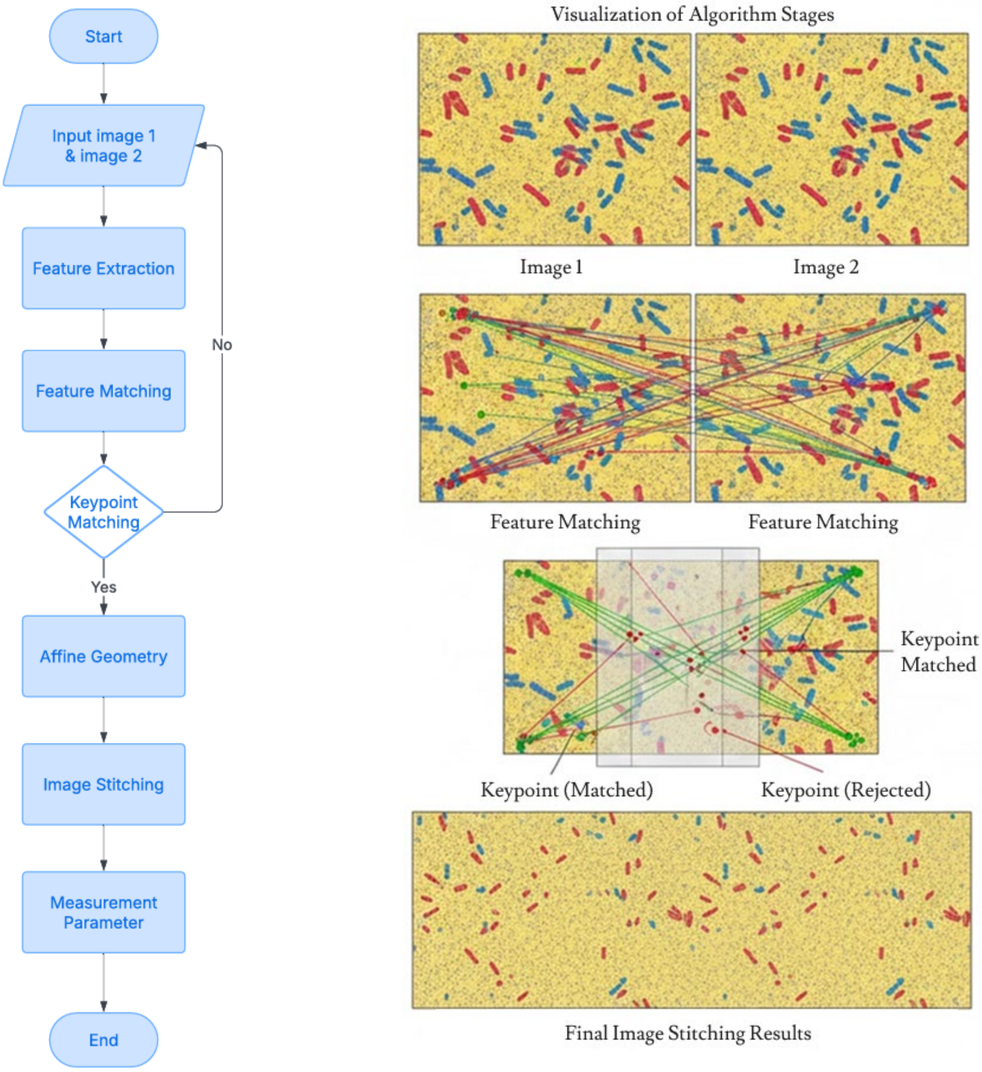

Fig. 1. The automated stitching pipeline for microscopic sputum images

Fig 1 show the automated stitching pipeline for microscopic sputum images: 1) The process begins with a pair of microscopic images that have already undergone feature detection using either SIFT or SURF algorithms, 2) A homography search is performed using the RANSAC algorithm, 3) A decision node evaluates the separation of matched keypoints, 4) Validated image pairs proceed to the Stitching and Optimization stage utilizing Affine Geometry, 5) The final phase involves calculating the Zero-Pixel count.

Two overlapping images taken from slightly different angles, each containing a 30-pixel overlap, are used as the starting point for the algorithm. In both images, the system identifies unique points of interest, or keypoints, as features. To identify commonalities, lines are drawn between corresponding features (keypoints matched). Keypoints (Matched) are legitimate points that are perfectly aligned between the two images in the overlapping region [35], [36]. Keypoints (Rejected) are points that don't make sense in the other image and are eliminated. Final automatic stitching results produce a smooth panoramic effect; the images are distorted and combined based on the matching keypoints.

2.2. Dataset Retrieval Process

Image acquisition was performed using an Olympus CX-31 microscope with a 100× oil-immersion objective integrated with a Canon EOS 700D DSLR camera to capture high-resolution morphological features of Mycobacterium tuberculosis. The dataset comprised digital JPG images from 2 cm × 1 cm sputum smears. Of the 100 captured overlapping images, 20 were selected for testing. The evaluation focused on two primary metrics: a ratio test to assess feature matching accuracy and zero-pixel analysis to quantify the seamlessness of the stitching outcome [15].

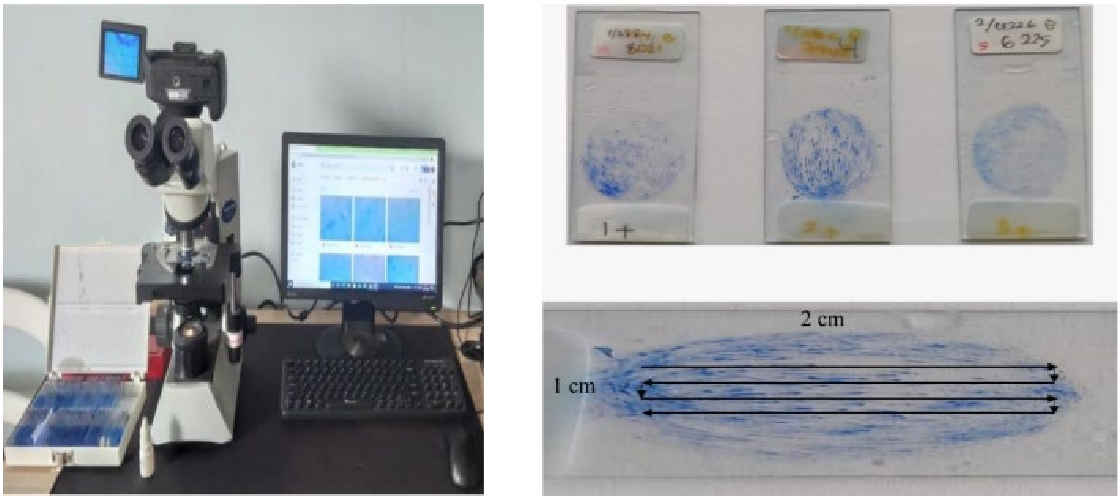

Fig. 2. Microscope Setup and Sputum Sample Preparation [4], [25].

2.3. Data Training & Data Testing

The system-processed microscopic images of tuberculosis sputum samples serve as the training and testing datasets for this study. A total of 80 images were utilized for the training phase, which was used to build and refine the automatic stitching workflow by teaching the algorithm to identify legitimate Keypoints (Matched) and discard Keypoints (Rejected). On the other hand, the testing dataset, which contains 20 images or 10 overlapping pairs in this study, is used as an independent validation set at the end for system evaluation and analysis.

To improve system robustness, an additional preprocessing step normalizing brightness and contrast was performed to minimize the impact of imaging variation. The dataset consists of a wide variety of sputum samples to provide and test the algorithm in realistic laboratory settings. This meticulous preparation helps ensure that both the training and testing stages closely mirror the real-world challenges of analyzing microscopic images.

2.4. Implementation of the SURF Algorithm in Image Stitching

After capturing the dataset, an automatic stitching process using the SURF algorithm is performed. In this setup, the program is programmed to run in Python, where the workflow looks like:

2.4.2. Preprocessing and Feature Extraction

Fig. 3 illustrates the overall workflow for preparing the image stitching dataset. The database is divided into 80 training images (40 overlapping pairs) and 20 testing images (10 overlapping pairs). Each image pair undergoes feature extraction, feature matching, keypoint matching with outlier rejection, and image stitching to generate the final panoramic image. The resulting stitched images are then used to train and evaluate the proposed model. Some classes from installed libraries will also be imported. To facilitate visual inspection, the image is first converted to greyscale (only grey levels). Feature extraction identifies local details in an image. In this situation, the SURF technique detects and describes such local features. SURF detects keypoints and produces descriptors that can be used for a wide range of analytic tasks, such as item matching, via `cv2.xfeatures2d.SURF_create()`.

2.4.3. Feature Matching

The `cv2.xfeatures2d.SURF_create()` having 400 as its Hessian threshold, 4 octaves, and 3 layers per octave. We used 64-dimensional descriptors, which provided faster processing while still retaining robust repeatability. Default settings were used for the SIFT method, with a contrast threshold of 0.04 and an edge threshold of 10. All the computations in the matching method used a Brute-Force Matcher with a distance metric, followed by the Ratio Test proposed by Lowe (0,7). The automatic stitching process employs RANSAC as a robust estimator (8-DOF) to extract and reject outliers in the feature matches. At this time, a (6-DOF) Affine geometric model is estimated by iteration using the inlier correspondences. This ensures that the final transformation accounts for the rotation, scaling, and translation inherent in high-magnification microscopy without being skewed by false matches.

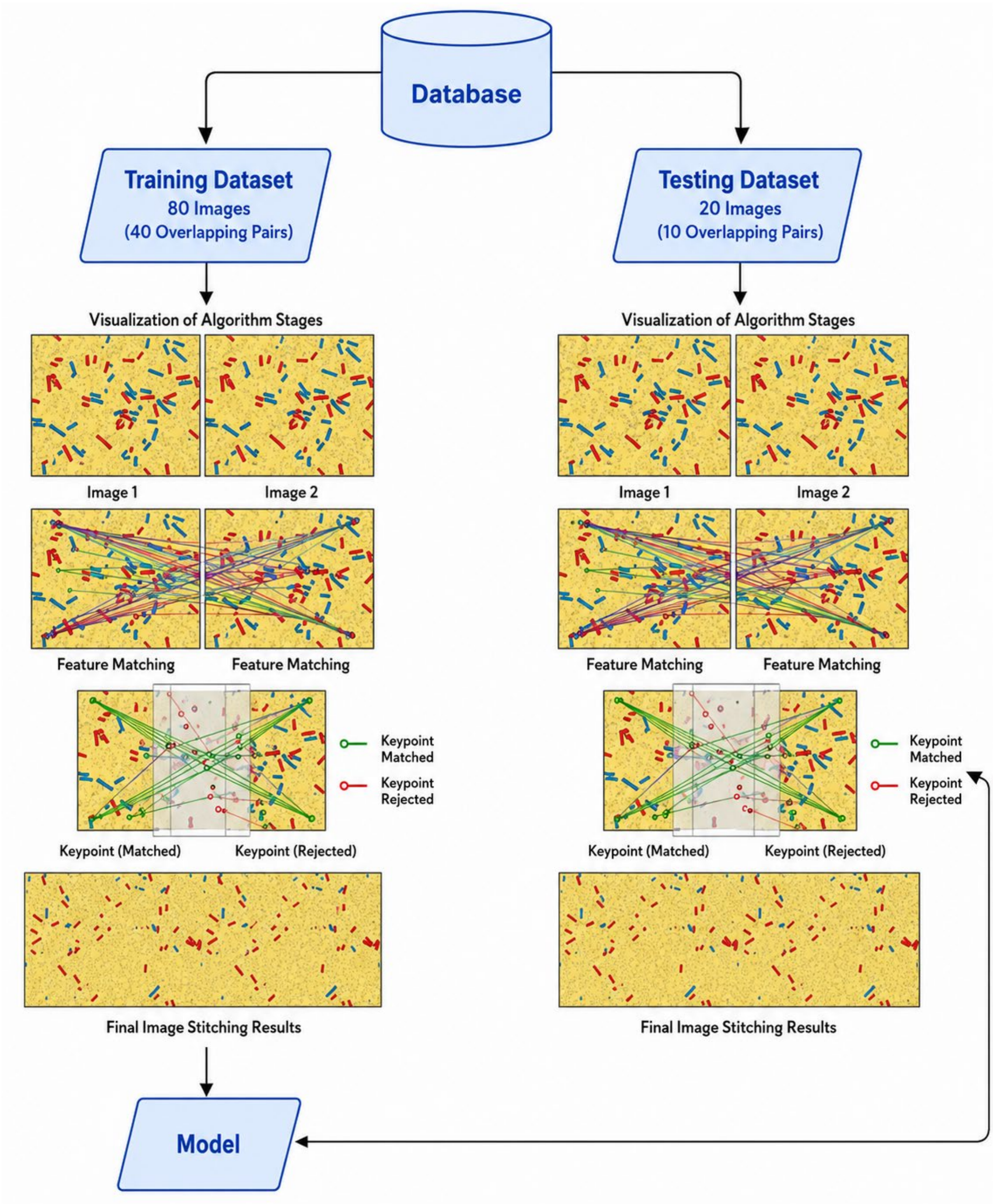

Fig. 3. Schematic Representation of The Training and Testing Dataset Workflow.

The aim of this step is to ascertain how similar or corresponding input images 1 and 2. Several algorithms, including the BF matcher, KNN, FLANN, and Lowe's Ratio Test, are used during the feature-matching phase [37]. By comparing key points or features in both input images, the flowchart illustrates how the image conducts feature search and then compares them to find the result, which is the level of image matching. The technique uses the closest-distance computation to find matches between keypoints. The system will draw a line if the final images are identical. The RANSAC algorithm is used in this procedure to separate keypoints and distinguish accurate matches from invalid ones [38], [39]. Fig. 4 and 6 show the entire automatic stitching process flow, and the image matching process is illustrated in Fig. 7.

Fig. 4 illustrates the preprocessing workflow for SURF-based feature extraction. The pipeline begins with connecting to Google Drive, installing the required libraries, importing the necessary modules, and loading the input image pair. The images are then converted from RGB to grayscale before applying the SURF algorithm to detect keypoints and compute their descriptors for subsequent feature matching and image stitching.

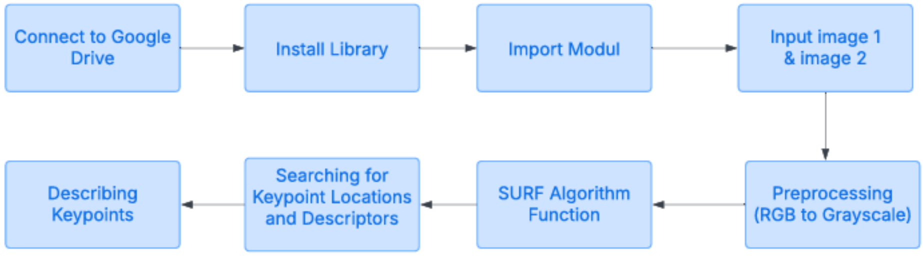

Fig. 4. Technical pipeline for microscopic image feature extraction (describing keypoints).

Fig. 5 illustrates the complete image-stitching workflow based on homography estimation and affine transformations. The process begins with a pair of input images that have already undergone keypoint detection and descriptor extraction. A homography matrix is then estimated using the Random Sample Consensus (RANSAC) algorithm to identify reliable feature correspondences while eliminating mismatched keypoints (outliers). If the number of valid matched keypoints is insufficient, the corresponding matches are rejected to prevent unreliable image alignment.

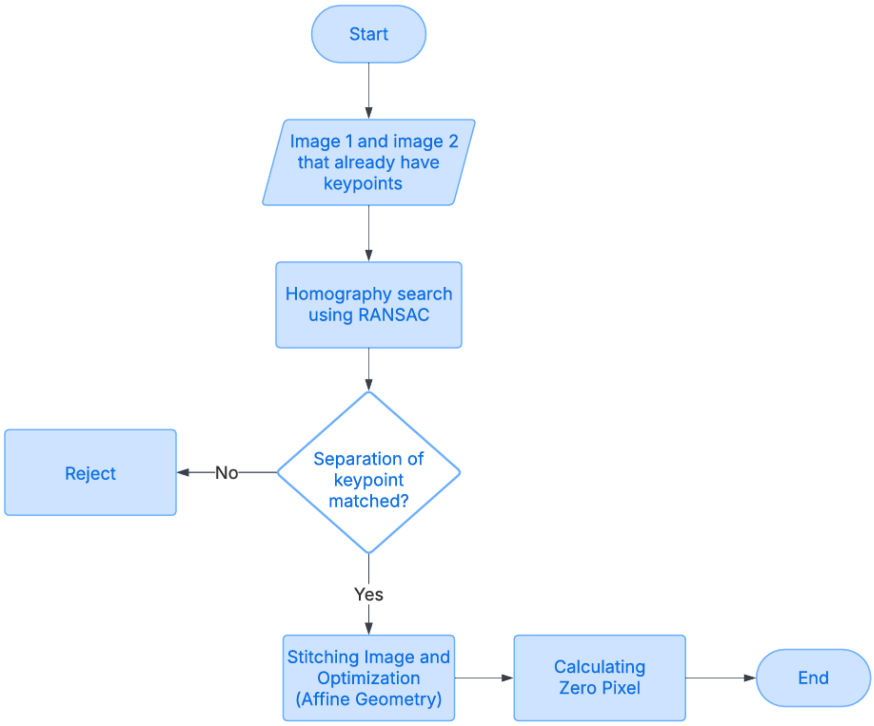

Fig. 5. Integrated Procedural Workflow for Feature Matching followed by a Homography search using the RANSAC algorithm

For successfully matched keypoints, the estimated homography is used to perform image alignment and stitching through affine geometric transformation. The stitched image is subsequently optimized to improve alignment quality and minimize visible artifacts. Finally, the number of zero-valued pixels in the stitched image is used as an objective metric to evaluate stitching quality, with fewer zero pixels indicating better overlap and more accurate image registration.

The workflow for image registration and automatic stitching is shown in Fig. 6. Initially, SIFT is employed to detect keypoints and extract local feature descriptors from the input image pair. The extracted descriptors are then matched using four feature matching strategies, namely Brute Force (BF), K-Nearest Neighbors (KNN), Fast Library for Approximate Nearest Neighbors (FLANN), and Lowe's Ratio Test, to identify reliable feature correspondences. If sufficient valid keypoint matches are obtained, the matched points are connected by lines to visualize the correspondence between the two images, indicating successful image registration. Otherwise, no connecting lines are drawn, signifying that the matching process did not satisfy the required correspondence criteria. Fig. 7 presents an example of keypoint matching between two sputum sample images.

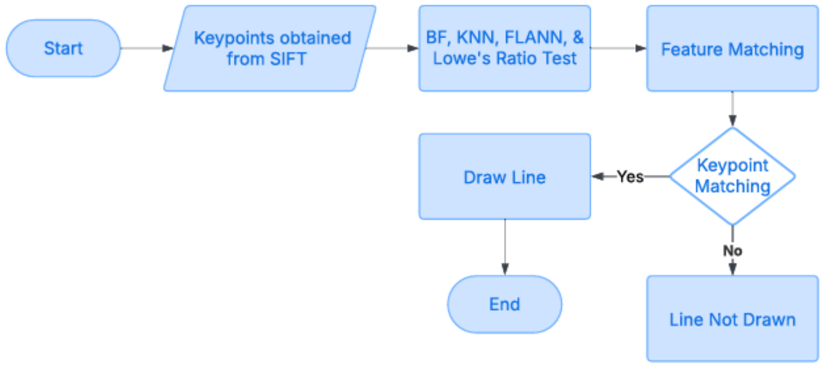

Fig. 6. Workflow of the Image Registration and Automatic Stitching Process.

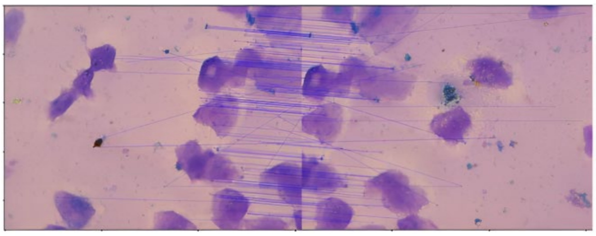

Fig. 7. Keypoint Matching Between Two Sputum Sample Images.

The automatic stitching result may contain black regions, which correspond to zero-pixel areas. These zero-pixel regions are measured and counted to quantify their occurrence, as shown in Fig. 8. This count is then used to determine the total number of zero-pixel areas in the merged image.

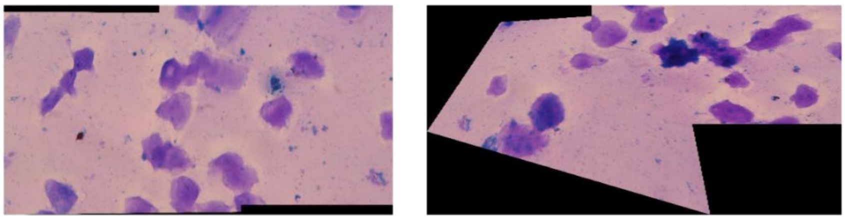

Fig. 8. (a). Successful automatic stitching result and (b). Failed automatic stitching result.

3. Results and Discussion

Testing was conducted using two scenarios to evaluate the effectiveness of the SURF algorithm in the automatic stitching process. Scenario-1 involved applying the ratio test with various ratios, while Scenario-2 focused on counting the number of zero-pixel (black) regions in the resulting stitched images. In both scenarios, 20 images were selected from a set of 100, ensuring that each contained overlapping areas. A ratio test (0,3 to 0,7) was conducted based on the distances between the two closest points. Suppose d1 and d2 (d1 < d2) are the distances from a point to the closest matching point. In this ratio test, keypoint matching for automatic stitching was performed using the SIFT and SURF algorithms, as in previous research [25]. Fig. 9 shows that keypoint matching using the SIFT algorithm achieves the highest effectiveness for all image pairs (success rate of 92%) when threshold ratios of 0,5 and 0,6 are applied. On the other hand, a total of 10 pairs of sputum images were successfully stitched using the SURF algorithm for all ratio values from 0.3 to 0.7. Based on Fig. 9, the overall success rate of automatic stitching with SURF is 100%.

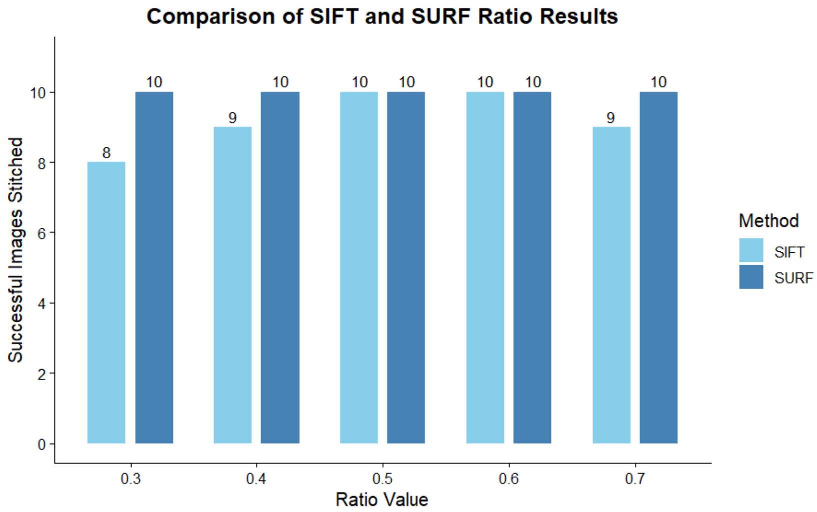

Fig. 9. Comparative Analysis of Success Rates between the SIFT Algorithm (Previous Research) and the Proposed SURF-based Framework.

The second test involved calculating the number of zero-pixel values in the image produced by the automatic stitching process. The absence of pixels in the stitching result is attributed to discrepancies between the canvas and the stitching output, with the canvas being larger than the stitching result. It is important to know how many such zero-pixel regions were obtained, since this number defines the minimum and maximum void sizes in the output composite. This measurement provides a direct evaluation of stitch quality and the system's performance in reducing gaps. The results of this zero-pixel analysis are summarized in Table 1, which presents representative 10-pair test images for the most favorable simulation outcomes for both types, with ratio tests and thresholds of (0,5) and (0,6).

Table 1. Zero pixel Calculation Result on SIFT and SURF Method.

No	Sample	Zero pixel				Proposed Method
		SIFT [29]		SURF		
		0,5 (SIFT)	0,6 (SIFT)	0,5 (SURF)	0,6 (SURF)	0,6
1	IMAGES 1278 & 1279	1.333.845	1.361.982	1.228.347	1.183.629	372.642
2	IMAGES 1280 & 1281	1.524.240	1.319.892	1.467.732	1.204.701	359.404
3	IMAGES 1282 & 1283	1.638.594	1.640.241	1.520.961	2.031.579	366.949
4	IMAGES 1296 & 1297	1.902.180	1.666.532	1.595.616	1.622.052	455.598
5	IMAGES 1302 & 1303	1.446.852	1.332.459	1.330.641	1.334.034	363.258
6	IMAGES 1314 & 1315	1.958.070	2.010.333	1.905.120	1.818.651	408.793
7	IMAGES 1316 & 1317	1.088.877	1.069.687	1.179.182	1.113.363	408.217
8	IMAGES 1318 & 1319	1.390.564	1.340.980	1.218.418	1.301.359	418.658
9	IMAGES 1320 & 1321	1.262.871	1.071.947	1.030.296	964.247	385.162
10	IMAGES 1334 & 1335	1.779.337	1.713.616	1.798.014	1.791.416	345.263
	Max Zero pixel	**1.958.070**	**2.010.333**	**1.905.120**	**2.031.579**	**455.598**
	Min Zero pixel	**1.088.077**	**1.069.687**	**1.030.296**	**964.247**	**345.263**

This information is necessary to verify that the feature extraction algorithm provides stability and accuracy for automatic stitching at agreed-upon threshold levels. The testing results indicated that, overall, the lowest values were recorded for the similar ratio settings of 0,5 and 0,6 when using the SURF algorithm (grey highlight) over the SIFT algorithm. Based on testing scenario one, the ratio test for stitching using the SIFT and SURF methods yielded different levels of accuracy. The accuracy of the ratio test for stitching using the SIFT method was 92%. Meanwhile, the ratio test results for stitching using the SURF method showed 100% accuracy, as shown in Table 2. In the second scenario (based on Table 1), the smallest zero-pixel minimum was obtained in the automatic stitching results using the SURF method. When compared to SIFT, the minimum number of zero pixels in SURF is lower, approaching 1,069.687 and 964.247, respectively.

A comparison between SIFT and SURF confirms a clear trade-off in automatic stitching quality. By contrast, SURF achieved a 100% stitching success rate across all 10 image pairs in the test data, suggesting more robust performance for automatic stitching. This computational advantage can be attributed to SURF's use of Haar wavelet responses and the Hessian determinant. While SIFT relies on a Difference of Gaussian (DoG) algorithm to highlight fine-grained intensity changes, SURF represents larger image structures with wavelet-based descriptors. Therefore, SURF is less sensitive to high-frequency noise and non-uniform illumination, as well as irregular and low-contrast structures, frequently found on Ziehl-Neelsen-stained MTB formations. Experimental results also corroborate this improvement: the SURF-affine pipeline produces significantly fewer alignment artifacts, with a total of 345.263 zero-pixels compared to 1.069.787 with SIFT.

Table 2. Comparison of SIFT and SURF Performance.

No	Parameter	SIFT Method	SURF Method
1	Accuracy Level	92%	100%
2	Zero-Pixel Count	Higher	Lower (Better Quality)
3	Robustness	Sensitive to viewing angles	Resistant to rotation, blurring, & angles
4	Feature Matching	Higher rate of Keypoint (Rejected)	More stable Keypoint (Matched)

4. Conclusion

Within this study, an automatic stitching approach was implemented and tested using a feature-based strategy for TB sputum images. Two algorithms (SIFT and SURF) were tested to evaluate their performance in generating seamless automatic stitching from microscopic sputum samples. While the panoramic images produced by both methods were identical, quantitative evaluation using the zero-pixel metric indicated that SURF-affine expansion achieved higher alignment accuracy than classical SIFT. Indeed, SURF-affine had a minimum zero-pixel value of 345.263, which was smaller than classical SIFT (1.069.687) and classical SURF (964.247). A limitation of this preliminary study is the missing RMSE measurements. Incorporating these quantitative measures is left for future work to obtain an in-depth evaluation of the geometric alignment, complementing our zero-pixel analysis. Although automatic stitching has made great progress, some issues persist. Smear quality, non-uniform illumination, and lack of overlap can limit the robustness of the stitching process. The next step will be to further validate our results on a larger dataset (e.g., positive tuberculosis cases) to confirm the generalizability of our methods for digital pathology and WSI applications. We also want to combine adaptive contrast normalization with improved overlap handling to reduce residual artefacts and improve the robustness of automated diagnostic systems.

Acknowledgment

Part of this research was supported through an Internal Research Grant from Telkom University.

Declarations

Author contribution. Nadya: Data collection, analysis, and programming. Indrarini and Suci Aulia: Data analysis and conceptualization. Lestari: Data analysis, article writing, and literature review. All authors participated in the final data analysis.
Funding statement. None of the authors have received any funding or grants from any institution or funding body for the research.
Conflict of interest. The authors declare no conflict of interest.

Additional information. No additional information is available for this paper.

References

[1] J. Chakaya *et al.*, "Global Tuberculosis Report 2020 – Reflections on the Global TB burden, treatment and prevention efforts," *Int. J. Infect. Dis.*, vol. 113, pp. S7–S12, Dec. 2021, doi: 10.1016/j.ijid.2021.02.107.

[2] N. Pamela Sari and A. S. Rachmawati, "Pendidikan Kesehatan Tuberkulosis 'TOSS TB (Temukan Obati Sampai Sembuh),'" *ABDIMAS J. Pengabdi. Masy.*, vol. 2, no. 1, pp. 103–107, Apr. 2019, doi: 10.35568/abdimas.v2i1.338.

[3] H.-T. Fu, H.-Z. Tu, H.-S. Lee, Y. E. Lin, and C.-W. Lin, "Evaluation of an AI-Based TB AFB Smear Screening System for Laboratory Diagnosis on Routine Practice," *Sensors*, vol. 22, no. 21, p. 8497, Nov. 2022, doi: 10.3390/s22218497.

[4] S. Aulia, A. B. Suksmono, T. R. Mengko, and B. Alisjahbana, "A Novel Digitized Microscopic Images of ZN-Stained Sputum Smear and Its Classification Based on IUATLD Grades," *IEEE Access*, vol. 12, pp. 51364–51380, 2024, doi: 10.1109/ACCESS.2024.3386208.

[5] M. R. Syahwana and R. M. Simanjorang, "Analisa Sistem Pakar Metode Bayes Dalam Mendiagnosa Penyakit Tubercolosis," *J. Sist. Informasi, Tek. Inform. dan Teknol. Pendidik.*, vol. 1, no. 2, pp. 57–66, Mar. 2022, doi: 10.55338/justikpen.v1i2.7.

[6] E. H. Tobin and D. Tristram, *Tuberculosis Overview*. StatPearls Publishing, 2024. Accessed: Jun. 20, 2026. [Online]. Available: https://www.ncbi.nlm.nih.gov/books/NBK441916/

[7] J. Long, H. E. Parker, K. Ehrlich, M. G. Tanner, K. Dhaliwal, and B. Mills, "Frugal filtering optical lenses for point-of-care diagnostics," *Biomed. Opt. Express*, vol. 11, no. 4, p. 1864, Apr. 2020, doi: 10.1364/BOE.381014.

[8] A. Ojha, S. Banik, S. K. Melanthota, and N. Mazumder, "Light emitting diode (LED) based fluorescence microscopy for tuberculosis detection: a review," *Lasers Med. Sci.*, vol. 35, no. 6, pp. 1431–1437, Aug. 2020, doi: 10.1007/s10103-019-02947-6.

[9] T. N. Susilawati and R. Larasati, "A recent update of the diagnostic methods for tuberculosis and their applicability in Indonesia: a narrative review," *Med. J. Indones.*, vol. 28, no. 3, pp. 284–91, Oct. 2019, doi: 10.13181/mji.v28i3.2589.

[10] Y. Zaizen *et al.*, "Deep-Learning-Aided Detection of Mycobacteria in Pathology Specimens Increases the Sensitivity in Early Diagnosis of Pulmonary Tuberculosis Compared with Bacteriology Tests," *Diagnostics*, vol. 12, no. 3, p. 709, Mar. 2022, doi: 10.3390/diagnostics12030709.

[11] G. Davidson *et al.*, "Overview of Tuberculosis: Causes, Symptoms and Risk Factors," *Asian J. Res. Infect. Dis.*, vol. 15, no. 9, pp. 8–19, Aug. 2024, doi: 10.9734/ajrid/2024/v15i9370.

[12] G. Bediang, B. Stoll, N. Elia, J.-L. Abena, and A. Geissbuhler, "SMS reminders to improve adherence and cure of tuberculosis patients in Cameroon (TB-SMS Cameroon): a randomised controlled trial," *BMC Public Health*, vol. 18, no. 1, p. 583, Dec. 2018, doi: 10.1186/s12889-018-5502-x.

[13] M. Hatherill, R. E. Chaisson, and C. M. Denkinger, "Addressing critical needs in the fight to end tuberculosis with innovative tools and strategies," *PLOS Med.*, vol. 16, no. 4, p. e1002795, Apr. 2019, doi: 10.1371/journal.pmed.1002795.

[14] K. Nurzynska, D. Li, A. E. Walts, and A. Gertych, "Multilayer outperforms single-layer slide scanning in AI-based classification of whole slide images with low-burden acid-fast mycobacteria (AFB)," *Comput. Methods Programs Biomed.*, vol. 234, no. June, p. 107518, Jun. 2023, doi: 10.1016/j.cmpb.2023.107518.

[15] H.-C. Huang, K.-L. Kuo, M.-H. Lo, H.-Y. Chou, and Y. E. Lin, "Novel TB smear microscopy automation system in detecting acid-fast bacilli for tuberculosis – A multi-center double blind study," *Tuberculosis*, vol. 135, no. July, p. 102212, Jul. 2022, doi: 10.1016/j.tube.2022.102212.

[16] H. D. T. G. Samarasinghe, L. L. R. Sampath, H. R. M. M. V. B. Thilakarathna, R. A. R. C. Gopura, T. D. Lalitharatne, and Y. W. R. Amarasinghe, "Development of an automated microscopic imaging system for TB screening," in *2016 Electrical Engineering Conference (EECon)*, IEEE, Dec. 2016, pp. 7–12. doi: 10.1109/EECon.2016.7830927.

[17] F. Yang, Z.-S. Deng, and Q.-H. Fan, "A method for fast automated microscope image stitching," *Micron*, vol. 48, no. May, pp. 17–25, May 2013, doi: 10.1016/j.micron.2013.01.006.

[18] K. A. Johnson and G. M. Hagen, "Artifact-free whole-slide imaging with structured illumination microscopy and Bayesian image reconstruction," *Gigascience*, vol. 9, no. 4, Apr. 2020, doi: 10.1093/gigascience/giaa035.

[19] G. Nikolaev, D. Korshunov, and A. Khvostikov, "Automatic stitching of panoramas for geological images of polished sections," *ISPRS Ann. Photogramm. Remote Sens. Spat. Inf. Sci.*, vol. X-2/W1-202, pp. 39–46, Dec. 2024, doi: 10.5194/isprs-annals-X-2-W1-2024-39-2024.

[20] N. K. EL Abbadi, S. A. Al Hassani, and A. H. Abdulkhaleq, "Panoramic Image Stitching Techniques Based on SURF and Singular Value Decomposition," in *Communications in Computer and Information Science*, vol. 1511 CCIS, Springer Science and Business Media Deutschland GmbH, 2021, pp. 63–86. doi: 10.1007/978-3-030-93417-0_5.

[21] E. Karami, M. Shehata, and A. Smith, "Image Identification Using SIFT Algorithm: Performance Analysis against Different Image Deformations," pp. 1–4, Mar. 2018, Accessed: Jun. 20, 2026. [Online]. Available: http://arxiv.org/abs/1710.02728.

[22] N. Kumar, R. Gupta, and S. Gupta, "Whole Slide Imaging (WSI) in Pathology: Current Perspectives and Future Directions," *J. Digit. Imaging*, vol. 33, no. 4, pp. 1034–1040, Aug. 2020, doi: 10.1007/s10278-020-00351-z.

[23] R. Miggiano, M. Rizzi, and D. M. Ferraris, "Mycobacterium tuberculosis Pathogenesis, Infection Prevention and Treatment," *Pathogens*, vol. 9, no. 5, p. 385, May 2020, doi: 10.3390/pathogens9050385.

[24] N. Chamidah, Y. S. Yonani, E. Ana, and B. Lestari, "Identification the number of Mycobacterium tuberculosis based on sputum image using local linear estimator," *Bull. Electr. Eng. Informatics*, vol. 9, no. 5, pp. 2109–2116, Oct. 2020, doi: 10.11591/eei.v9i5.2021.

[25] N. G. Anggana, I. D. Irawati, S. Aulia, and Lestari, "Stitching Microscopic Images for Tuberculosis Sputum Samples," *J. Innov. Image Process.*, vol. 7, no. 4, pp. 1168–1185, Oct. 2025, doi: 10.36548/jiip.2025.4.005.

[26] J. Lockhart, S. Assefa, A. Alajdad, A. Alexander, T. Balch, and M. Veloso, "SURF: improving classifiers in production by learning from busy and noisy end users," in *Proceedings of the First ACM International Conference on AI in Finance*, New York, NY, USA: ACM, Oct. 2020, pp. 1–8. doi: 10.1145/3383455.3422547.

[27] D. Mistry and A. Banerjee, "Comparison of Feature Detection and Matching Approaches: SIFT and SURF," *Glob. Res. Dev. Journals*, vol. 2, no. 4, pp. 7–13, May 2025, doi: 10.70179/3qhg4p03.

[28] W. Y. Sulistyo, I. Riadi, and A. Yudhana, "Penerapan Teknik SURF pada Forensik Citra untuk Analisa Rekayasa Foto Digital," *JUITA J. Inform.*, vol. 8, no. 2, p. 179, Nov. 2020, doi: 10.30595/juita.v8i2.6602.

[29] P. Kaur, N. Kumar, and M. Singh, "SURFBCS: speeded up robust features based fuzzy vault scheme in biometric cryptosystem," *J. Supercomput.*, vol. 79, no. 11, pp. 12292–12316, Jul. 2023, doi: 10.1007/s11227-023-05142-1.

[30] N. K. EL Abbadi, S. A. Al Hassani, and A. H. Abdulkhaleq, "A Review Over Panoramic Image Stitching Techniques," *J. Phys. Conf. Ser.*, vol. 1999, no. 1, p. 012115, Sep. 2021, doi: 10.1088/1742-6596/1999/1/012115.

[31] X. Chen, J. Li, and Y. Sui, "A New Stitching Method for Dark-Field Surface Defects Inspection Based on Simplified Target-Tracking and Path Correction," *Sensors*, vol. 20, no. 2, p. 448, Jan. 2020, doi: 10.3390/s20020448.

[32] Z. Hu, G. Xu, L. Chen, N. Fu, and S. Zhen, "Error matching elimination based on a local affine algorithm," *J. Phys. Conf. Ser.*, vol. 2216, no. 1, p. 012075, Mar. 2022, doi: 10.1088/1742-6596/2216/1/012075.

[33] Y. Tang, S. Tian, P. Shuai, and Y. Duan, "MGHE-Net: A Transformer-Based Multi-Grid Homography Estimation Network for Image Stitching," *IEEE Access*, vol. 12, pp. 49216–49227, 2024, doi: 10.1109/ACCESS.2024.3384598.

[34] Y. Riwanto, M. T. Nuruzzaman, S. Uyun, and B. Sugiantoro, "Data Search Process Optimization using Brute Force and Genetic Algorithm Hybrid Method," *IJID (International J. Informatics Dev.*, vol. 11, no. 2, pp. 222–231, Jan. 2023, doi: 10.14421/ijid.2022.3743.

[35] I. Hadi Ali and S. Salman, "360-Degree Panoramic Image Stitching for Un-ordered Images Based on Harris Corner Detection," *Indian J. Sci. Technol.*, vol. 12, no. 4, pp. 1–9, Jan. 2019, doi: 10.17485/ijst/2019/v12i4/140988.

[36] H. Singh, *Practical Machine Learning and Image Processing*. Berkeley, CA: Apress, 2019. doi: 10.1007/978-1-4842-4149-3.

[37] M. Tuli, K. Kamali, and D. B. Lindell, "Generative Panoramic Image Stitching," Jul. 2025, Accessed: Jun. 20, 2026. [Online]. Available: http://arxiv.org/abs/2507.07133.

[38] S. Rabby and S. M. Masudul Ahsan, "Copy-Move Forgery Detection Utilizing SIFT and FLANN with Optimized Keypoint Matching," in *2024 27th International Conference on Computer and Information Technology (ICCIT)*, IEEE, Dec. 2024, pp. 2237–2242. doi: 10.1109/ICCIT64611.2024.11022130.

[39] S. Venezia, S. Coleman, D. Kerr, and J. Fegan, "Feature-based Approaches to Multi-View Image Stitching," in *2025 IEEE Symposium on Computational Intelligence in Image, Signal Processing and Synthetic Media Companion (CISM Companion)*, IEEE, Mar. 2025, pp. 1–5. doi: 10.1109/CISMCompanion65074.2025.11033067.